Low-mass runaways from the Orion Nebula Cluster – kinematic age constraints on star cluster formation

Monthly Notices of the ROYAL ASTRONOMICAL SOCIETY

MNRAS **537,** 1320–1333 (2025)
Advance Access publication 2025 January 20

https://doi.org/10.1093/mnras/staf074

Low-mass runaways from the Orion Nebula Cluster – kinematic age constraints on star cluster formation

Muhammad Fajrin,[1,2] Joseph J. Armstrong ,[2]★ Jonathan C. Tan,[2,3] Juan P. Farias [4] and Laurent Eyer[5]

[1]*Astronomy Study Program, Faculty of Mathematics and Natural Sciences, Institut Teknologi Bandung, Jalan Ganesha 10, Bandung 40132, Indonesia*
[2]*Department of Space, Earth & Environment, Chalmers University of Technology, SE-412 96 Gothenburg, Sweden*
[3]*Department of Astronomy, University of Virginia, Charlottesville, VA 22904, USA*
[4]*Department of Astronomy, University of Texas, Austin, TX 78712, USA*
[5]*Department of Astronomy, University of Geneva, Chemin Pegasi 51, CH-1290 Versoix, Switzerland*

Accepted 2025 January 6. Received 2024 November 25; in original form 2024 February 19

ABSTRACT

In their early, formative stages star clusters can undergo rapid dynamical evolution leading to strong gravitational interactions and ejection of "runaway" stars at high velocities. While O/B runaway stars have been well studied, lower-mass runaways are so far very poorly characterized, even though they are expected to be much more common. We carried out spectroscopic observations with MAG2-MIKE to follow-up 27 high priority candidate runaways consistent with having been ejected from the Orion Nebula Cluster (ONC) > 2.5 Myr ago, based on *Gaia* astrometry. We derive spectroscopic youth indicators (Li and H α) and radial velocities, enabling detection of bona fide runaway stars via signatures of youth and 3D traceback. We successfully confirmed 11 of the candidates as low-mass Young Stellar Objects (YSOs) on the basis of our spectroscopic criteria and derived radial velocities (RVs) with which we performed 3D traceback analysis. Three of these confirmed YSOs have kinematic ejection ages > 4 Myr, with the oldest being 4.7 Myr. Assuming that these stars indeed formed in the ONC and were then ejected, this yields an estimate for the overall formation time of the ONC to be at least ~ 5 Myr, i.e. about 10 free-fall times, and with a mean star formation efficiency per free-fall time of $\bar{\epsilon}_{\rm ff} \lesssim 0.05$. These results favour a scenario of slow, quasi-equilibrium star cluster formation, regulated by magnetic fields and/or protostellar outflow feedback.

Key words: techniques: spectroscopic – surveys – stars: kinematics and dynamics – stars: pre-main-sequence – open clusters and associations: individual: Orion Nebula Cluster.

1 INTRODUCTION

Stars tend to form in clusters from dense gas clumps within giant molecular clouds (GMCs) (Lada & Lada 2003). In their early, gas-dominated stages, they may undergo significant dynamical evolution, which can lead to regions of enhanced stellar densities, mass segregation, processing of multiple systems, and ejection of 'runaway' or 'walkaway' stars (e.g. Marks & Kroupa 2012; Parker et al. 2014; Farias, Tan & Chatterjee 2019). The kinematic 'ejection age' of such stars can provide an important constraint on the age of a cluster, which is independent and complementary to ages based on pre-main-sequence stellar evolutionary models. In particular, the oldest ejected runaways from a cluster offer model independent lower limits on cluster age. For a still forming cluster, the cluster age gives a lower limit on the age spread of the system and thus an upper limit on the time averaged star formation rate (SFR), or equivalently the star formation efficiency per free-fall time ($\bar{\epsilon}_{\rm ff}$). This is a basic parameter that can help distinguish different theoretical models of star cluster formation, i.e. between those involving 'fast' formation within one or a few free-fall times (e.g. Elmegreen et al. 2000) and those assuming 'slow', quasi-equilibrium formation (e.g. Tan, Krumholz & McKee 2006). Furthermore, the fraction of stars that become runaways depends sensitively to the duration of the dense, early, gas-rich phase (Oh & Kroupa 2016; Farias et al. 2019). So an accurate assessment of this time-scale from finding oldest known runaways enables a more accurate prediction of the global runaway population.

Most known runaway stars are bright O- and B-type stars (e.g. Tetzlaff, Neuhäuser & Hohle 2011), since they are easier to observe than fainter, lower-mass stars. However, *N*-body simulations (e.g. Farias et al. 2019; Schoettler et al. 2019) predict that most runaway stars will be of low mass. With the availability of high-precision 5-parameter astrometry from *Gaia* (Gaia Collaboration 2021), we are now able to extend our search for runaways to these numerous low-mass stars too. However, with only plane of sky proper motion and spatial information that enables a '2D-traceback' type analysis, there are generally many field star interlopers that can masquerade as runaway candidates (e.g. Farias, Tan & Eyer 2020). Radial velocity information can help reduce this contamination, but current *Gaia* releases do not provide radial velocities (RVs) for relatively faint stars, and those that are available have large uncertainties ($\sim$15 km s^{-1} for sources with $V = 15.7$ mag). To analyse the full 3D velocities of low-mass candidate runaways, it is necessary to

★ E-mail: joseph.armstrong@chalmers.se

combine *Gaia* astrometry with spectroscopic radial velocities. The same spectroscopic observations can also yield indicators of stellar youth, e.g. H α emission or Li absorption, which are then the key tests for secure identification of a low-mass runaway star from a young cluster.

The Orion Nebula Cluster (ONC) is the nearest dense ($> 10^4$ $M_\odot$ pc^{-3}; see Hillenbrand 1997) cluster that is still forming stars ($\sim$400 pc; e.g. Kuhn et al. 2019, $\sim$4 Myr; e.g. Da Rio et al. 2016), making it an important test case for theories of star cluster formation. Recent studies have identified high velocity stars consistent with having been ejected from the ONC (McBride & Kounkel 2019; Farias et al. 2020; Platais et al. 2020; Schoettler et al. 2020; Bobylev & Bajkova 2021), but these works lacked precise radial velocities for the majority of their runaway candidates and so have been largely limited to analysis in 2D. In particular, Farias et al. (2020) used *Gaia* DR2 proper motions to search for runaway candidates in a 45° radius around the ONC, in combination with *Gaia* and *WISE* photometric classifications (Marton et al. 2019) and optical variability (Cody & Hillenbrand 2014), to identify young stellar objects (YSOs) consistent with the age of the ONC. Using their best candidates, Farias et al. (2020) constructed a high velocity distribution for the ONC that was compared with *N*-body simulations, showing that the dynamical history of the ONC is consistent with a dense primordial environment (with mass surface densities of $\sim$1 g cm^{-2}) and low star formation efficiency per free fall time ($\sim$1 per cent). However, only 7 per cent of their proper motion candidates had measured radial velocities with which full 3D traceback could be calculated. Fewer than a third of sources with radial velocities had 3D traceback ages within 1 Myr of their 2D traceback ages, further highlighting the need for precise radial velocities. Therefore, it is imperative that the estimated high-velocity distribution of the ONC is cleaned of contaminants in order to determine the best cluster formation models that can reproduce it.

Even one single confirmed runaway would represent a breakthrough in extending the age estimate of the ONC via the ejection age method beyond the $\sim$2.5 Myr set by μ Col & AE Aur (Hoogerwerf, de Bruijne & de Zeeuw 2001), yielding crucial constraints on cluster formation models (Tan et al. 2006; Farias et al. 2019). For this project, we have selected the 27 highest priority targets from the Farias et al. (2020) candidate list updated with *Gaia* EDR3 astrometry, i.e. being relatively bright and with 2D traceback ages $>$ 2.5 Myr. We have carried out spectroscopic observations with MAG2-MIKE to follow-up these candidate runaways in order to confirm their youth with spectroscopic indicators (i.e. Li and H α) and to derive radial velocities to enable 3D-traceback to determine the likelihood of their origin in the ONC and the time of their ejection.

2 OBSERVATIONAL METHODS

2.1 Target selection

To select targets for spectroscopic follow-up, we updated the Farias et al. (2020) list of 16 994 candidate runaways with *Gaia* EDR3 astrometry, which has typical improvements in precision of proper motion by 33 per cent and parallax by 50 per cent compared to *Gaia* DR2 (Lindegren et al. 2021). We then re-calculated traceback parameters, such as 2D (plane of sky) closest approach to the ONC, ejection velocity in 2D, and traceback time to closest approach for candidates with reliable *Gaia* EDR3 astrometry (RUWE $<$1.4).

We cross-matched our candidate runaway list with the *Gaia* DR3 variable YSO catalogue (Marton et al. 2023; Rimoldini et al. 2023) to use this as another youth indicator. We also cross-matched the sample with the radial velocity compilation from *Survey of Surveys* (Tsantaki et al. 2022) to recalculate the 3D traceback for those targets with known RVs.

Runaway candidates were selected for spectroscopic observations if they passed two or more youth criteria (YSOflag, WYSOflag, VARflag, or *Gaia* DR3 variable YSO match, see Farias et al. 2020), had an 84th percentile predicted 3D traceback time ($t_{3D\ opt}$) greater than 2.5 Myr, a 2D closest approach consistent with originating within the cluster radius (10 arcmin corresponding to 1.2 pc, Farias et al. 2020), an ejection velocity (v_{t0}) greater than 4 km s^{-1}, and an estimated mass/$T_{\rm eff}$ (based on position in a *Gaia* colour–magnitude diagram) consistent with being in the mass range where Li is an effective youth indicator (e.g. Soderblom 2010). In the 2D traceback calculations we account for the peculiar motion of the Sun using velocities from Schönrich, Binney & Dehnen (2010). In total this gives us 27 candidate runaways for spectroscopic follow-up (Table 1). In Fig. 1, we illustrate how the candidates are spread across the sky. We will refer the candidates based on their identifiers in this table for ease of reference.

2.2 Observations

Observations took place on the 2022 December 16th and 2023 February 22 using the Magellan Inamori Kyocera Echelle (MIKE) spectrograph on Magellan-Clay 2 at Las Campanas Observatory (LCO). The 1.0 arcsec slit with 2 × 2 binning was used, yielding $R \sim$ 22 000 in the red and $R \sim$ 28 000 in the blue, respectively. All spectra cover the wavelength range from $\sim$3860 to $\sim$9000 Å. Exposure times were estimated for each star using the LCO exposure time calculator to achieve a combined SNR $>$ 20 from 3 exposures, allowing us to measure RVs and equivalent widths of Li and H α.

For each target, Th–Ar lamp exposures were taken as well as a set of 10 milky flats at the beginning of the night. Targets were observed in a slit pair mode, where that target spectrum is observed in one slit while a sky spectrum is observed in the other. Between multiple exposures the slits used for the target and the sky spectrum are alternated.

2.3 Data reduction

The spectroscopic data were reduced according to standard procedures using `IRAF`. The processes include data cleaning (flat-fielding, cosmic ray removal, and sky subtraction), spectral/aperture extraction, and wavelength calibration using Th–Ar comparison spectra. The reduction process resulted in multi-order spectra, which then were merged into a single spectrum and normalizeded using `IRAF` task `continuum` and `scombine`.

3 RESULTS

3.1 Signatures of youth

The youth signatures for the targets in general are predefined in Table 1 under the column labelled 'score', which are described in the caption (see Farias et al. 2020, for further details about how these were derived). In Table 1, we can see that all the targets either satisfy all the youth signatures or only fail in one. Also, this 'failure' can be due to the source not being able to be evaluated in this metric, such as the lack of IR photometry needed to evaluate the WYSOflag for 75 per cent of all candidates (Farias et al. 2020). Therefore, we expect that the selected targets do already have a high likelihood of being YSOs. Here, we report on their additional youth indicators of

Table 1. List of candidate runaways observed with MAG2-MIKE. Columns are: Target identifier in the observation, *Gaia* DR3 ID number, Galactic longitude (*Gaia* DR3), Galactic latitude (*Gaia* DR3), *Gaia* DR3 *G*mag, *Gaia* YSO flag (Marton et al. 2023; Rimoldini et al. 2023), v_r from (a) *Gaia*, and (b) APOGEE taken from Tsantaki et al. (2022), Farias et al. (2020) score for youth criteria met ('a' for sources that pass the YSOflag criteria, 'b' for sources that only fail one of either YSOflag, WYSOflag, or VARflag criteria, 'I' for sources that pass both WYSOflag and VARflag criteria, 'II' for sources that pass either WYSOflag or VARflag criteria, '∗' for sources whose 2D closest approach overlaps with the center of the ONC within 1σ uncertainty, '!' for sources which fail the RVflag criteria), 2D ejection velocity (Farias et al. 2020), 2D closest approach to the ONC (Farias et al. 2020), 'optimal' 3D traceback time (Farias et al. 2020), exposure time per source.

ID	*Gaia* ID	ℓ (°)	b (°)	G mag	*Gaia* YSO	v_r (km s^{-1})	Score	v_{t0} (km s^{-1})	CA (arcmin)	$t_{3D,\mathrm{opt}}$ (Myr)	Exposure time (s)
OBJ-1	4844159373956999936	242.3397	−47.6840	15.26			bl∗!	37.58	15.76	$4.13^{+2.64}_{-1.86}$	3 × 250
OBJ-2	3192134597649605376	203.0002	−38.5044	16.47	✓		al	21.01	8.64	$5.14^{+0.85}_{-2.12}$	3 × 500
OBJ-3	4817925576274600192	242.0673	−39.4966	16.26			bl∗!	63.10	23.92	$3.82^{+0.62}_{-1.79}$	3 × 450
OBJ-4	3212944607551376384	203.9799	−24.5334	16.99			bl!	17.08	0.17	$3.05^{+1.31}_{-1.79}$	3 × 600
OBJ-5	3207501131641282176	208.2989	−24.6643	16.52			al	5.57	10.06	$5.23^{+6.15}_{-2.57}$	3 × 550
OBJ-6	3208291783581908608	208.0032	−24.2580	16.89	✓	$32.485 \pm 3.562^{(a)}$	bl	5.62	9.81	$4.56^{+5.30}_{-1.21}$	3 × 600
OBJ-7	3207022053810350976	209.2567	−24.7423	16.68	✓		al	6.68	12.82	$4.19^{+1.39}_{-1.95}$	3 × 550
OBJ-8	2957497235735128448	228.0767	−28.1871	16.99			bl∗	45.03	5.43	$2.43^{+1.51}_{-1.17}$	3 × 600
OBJ-9	2984454031031531008	217.6080	−23.1807	15.40			al∗!	8.07	16.43	$5.57^{+0.73}_{-2.79}$	3 × 250
OBJ-10	3216889827071056896	206.3162	−18.0608	16.46	✓		bl	12.19	6.71	$1.68^{+1.29}_{-0.94}$	3 × 500
OBJ-11	3215804677813294976	207.5906	−18.0482	16.81	✓		bl	8.53	9.10	$1.42^{+1.38}_{-0.78}$	3 × 600
OBJ-12	3012142379518284288	213.5078	−20.4489	15.37			bl∗	9.77	4.56	$2.56^{+1.20}_{-1.37}$	3 × 250
OBJ-13	3015308629408804608	212.7895	−19.7749	14.51		$39.946 \pm 0.702^{(b)}$	bl∗!	8.35	0.13	$2.88^{+0.79}_{-1.89}$	3 × 150
OBJ-14	3219378365481960832	204.7270	−15.0406	14.96			bl	8.60	13.72	$4.12^{+2.39}_{-2.04}$	3 × 150
OBJ-15	3216174629116142336	207.9220	−16.3723	14.39	✓		bl	10.93	13.28	$1.74^{+1.92}_{-0.78}$	3 × 100
OBJ-16	2888109908763598976	241.3582	−27.7466	15.39			al∗!	26.29	8.97	$4.79^{+2.81}_{-1.49}$	3 × 250
OBJ-17	3011187006993509504	215.0589	−18.3087	15.22			bl∗!	26.98	9.18	$1.67^{+1.23}_{-1.21}$	3 × 250
OBJ-18	3316420643274767488	204.2695	−10.1560	15.65			bl!	25.87	20.00	$3.81^{+1.51}_{-2.46}$	3 × 350
OBJ-19	3315632671394273024	204.7219	−9.4776	13.48		$107.556 \pm 1.452^{(a)}$	bll	33.08	18.13	$2.19^{+1.16}_{-1.27}$	3 × 80
OBJ-20	3018141830356350976	214.7763	−12.9386	16.31			bl!	30.53	18.15	$2.14^{+1.77}_{-1.34}$	3 × 450
OBJ-21	2932903703242234112	230.9026	−6.7062	12.30		$87.791 \pm 1.043^{(a)}$	bll∗!	21.96	34.66	$4.12^{+2.40}_{-3.68}$	3 × 50
OBJ-22	3017382033474172800	209.0747	−18.8395	14.18	✓		bl	4.47	2.22	$1.01^{+2.40}_{-0.69}$	3 × 100
OBJ-23	3023944262453551232	208.6032	−16.1726	14.90			bl	11.27	10.71	$1.91^{+2.16}_{-0.99}$	3 × 150
OBJ-24	2915784994393795456	227.9664	−23.0595	15.66			bl∗!	49.27	17.32	$3.20^{+1.50}_{-1.73}$	3 × 350
OBJ-25	2885209740687428224	243.5372	−22.5201	15.46			bl∗!	42.56	9.85	$3.73^{+2.15}_{-1.20}$	3 × 300
OBJ-26	3317517165606496256	205.4203	−5.6509	16.01			bl!	38.11	4.14	$2.88^{+1.78}_{-1.59}$	3 × 450
OBJ-27	5709959085012172928	239.3071	13.3290	16.43		$79.343 \pm 1.249^{(a)}$	bl!	66.91	19.63	$3.45^{+1.70}_{-1.58}$	3 × 500

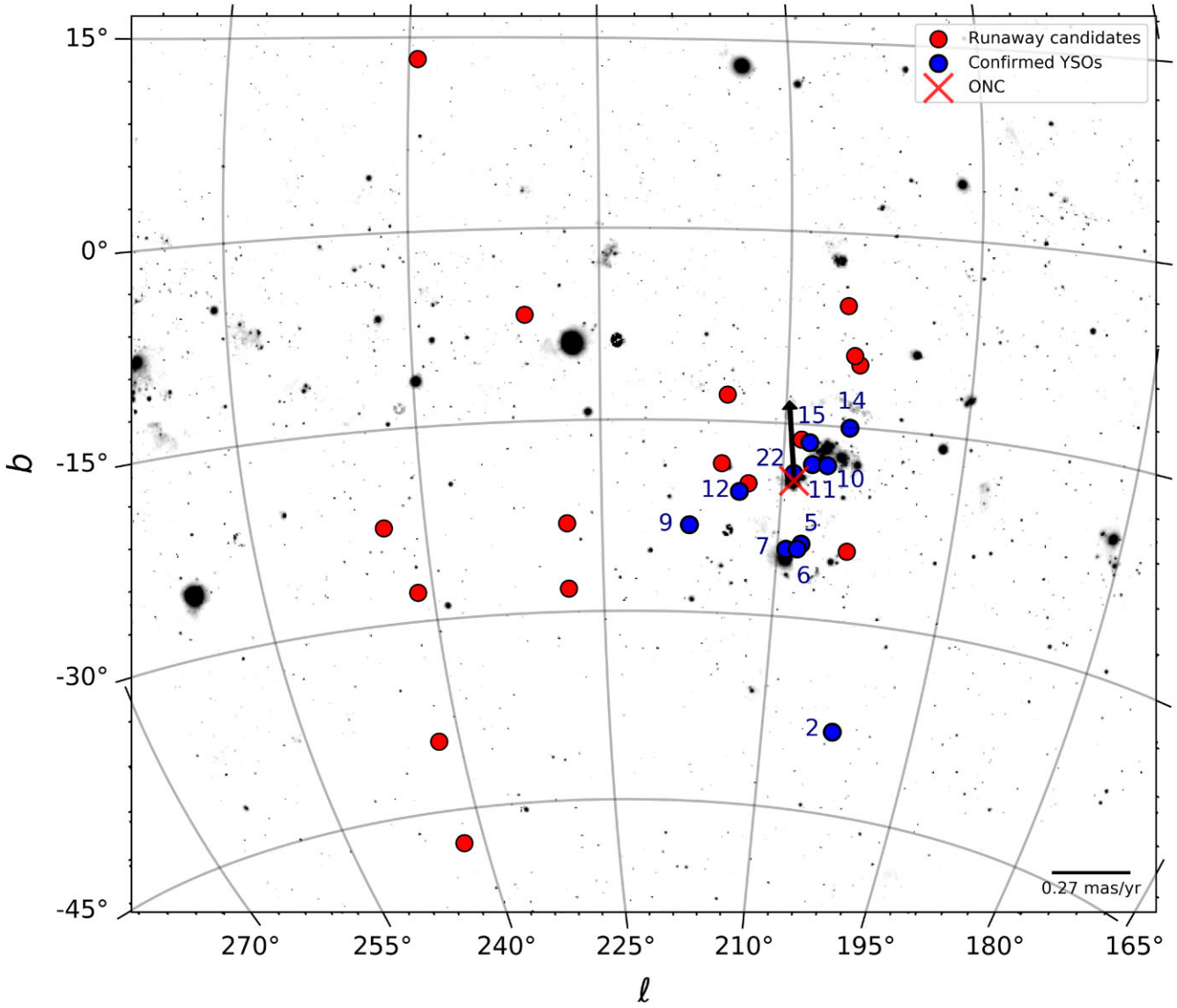

Figure 1. Spatial distribution of the 27 candidate runaways for spectroscopic follow-up. Those candidates with detected Li absorption, i.e. most likely to be YSOs, are coloured blue. The '*x*' symbol indicates the location of the ONC. The arrow indicates the proper motion of the ONC and the magnitude scale (mas yr^{-1}) of proper motion vector is indicated by the scale bar in the bottom right. The background is DSS2 Blue map of region around the ONC accessed from ALADIN.

Li and H α (Fig. 2) and then further examine their *Gaia* variability properties and their degree of IR excess.

Since we do not have multi-epoch spectra for our targets, we cannot rule out the possibility that some may be spectroscopic binaries. However, runaway stars ejected by dynamical disruption of multiple systems are expected to be predominantly single stars (Leonard & Duncan 1990; Perets & Šubr 2012; Schoettler 2022). It is also unlikely that a spectroscopic binary system will have an observed radial velocity that happens by chance to be consistent with ejection from the ONC. Therefore, we continue our analysis assuming that these are single stars.

3.1.1 *Li and H α equivalent widths*

Stars with high levels of magnetic activity (and therefore young) should exhibit hydrogen emission features. The youngest stars may also have ongoing accretion. The presence of lithium in the photospheres of low-mass stars can also be used to identify young stars (Soderblom 2010). Low-mass, fully convective stars are particularly efficient at burning lithium, which would then no longer be visible in the photosphere after a certain time. If the EW of the lithium 6708 Å line in such stars is several hundred mÅ the star is likely to be younger than 20–30 Myr.

We therefore look for the presence of H α and Li 6708 Å in the spectra of the observed candidates. We measure the equivalent widths of H α and Li 6708 Å using `IRAF` task `splot`, where we fit the lines with Gaussian profiles. The measurements are done for the individual exposures of each source and we then calculate the mean EW value for every star. Uncertainties were calculated using the Cayrel formula (Cayrel 1988), which assumes a Gaussian line profile and depends on the full width at half-maximun of the line, on the pixel size (in wavelength units) and on the S/N ratio. Measured equivalent-widths and their respective uncertainties are given in Table 2.

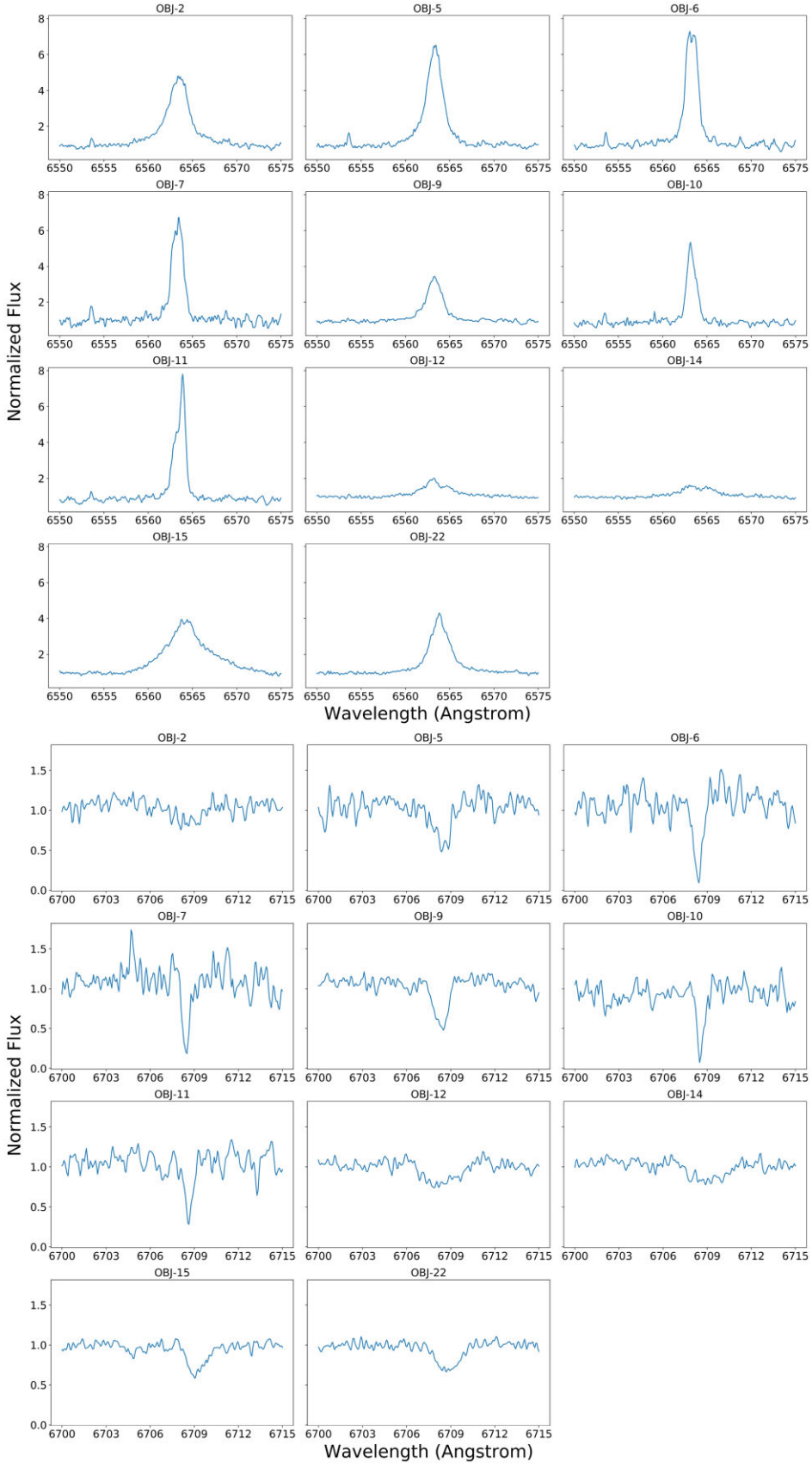

Figure 2. H α emission (*top)* and lithium 6708 Å (*bottom*) profiles in combined spectra of selected candidates. The fluxes are normalized non-calibrated counts.

Table 2. Results of spectral and traceback analysis for targets with spectroscopic youth indicators. Columns are; *Gaia* DR3 unique ID number, equivalent width of Li, equivalent width of H α, heliocentric radial velocity, time since closest approach to the ONC, distance of closest approach to the ONC, Farias et al. (2020) score for youth criteria met and flag for traceback consistent with originating from the ONC.

ID	*Gaia* ID	EW(Li) (mÅ)	EW(H α) (mÅ)	v_r (km s^{-1})	$v_{3D,ONC}$ (km s^{-1})	$\tau_{min,3D}$ (Myr)	$D_{min,3D}$ (pc)	Score	Bonafide
OBJ-2	3192134597649605376	750 ± 82	13260 ± 99	20.56 ± 0.43	31.17	4.40 ± 0.27	0.25 ± 6.69	aI	✓
OBJ-5	3207501131641282176	600 ± 75	15400 ± 104	15.87 ± 0.42	13.42	2.57 ± 0.80	19.47 ± 7.01	aI	
OBJ-6	3208291783581908608	616 ± 68	13700 ± 105	16.96 ± 0.42	12.84	4.34 ± 1.07	2.32 ± 9.09	bI	✓
OBJ-7	3207022053810350976	529 ± 87	9310 ± 126	14.96 ± 1.02	15.26	3.19 ± 0.72	8.01 ± 6.81	aI	✓
OBJ-9	2984454031031531008	643 ± 42	6220 ± 57	19.78 ± 1.01	15.06	4.68 ± 0.31	5.02 ± 3.11	aI*	✓
OBJ-10	3216889827071056896	440 ± 102	5425 ± 127	31.44 ± 2.73	13.38	1.52 ± 0.92	1.67 ± 10.57	bI	✓
OBJ-11	3215804677813294976	513 ± 62	10510 ± 86	3.54 ± 0.81	25.16	1.08 ± 0.71	4.28 ± 18.59	bI	✓
OBJ-12	3012142379518284288	810 ± 62	4560 ± 77	21.88 ± 2.42	14.13	2.22 ± 0.46	4.28 ± 7.09	bI*	✓
OBJ-14	3219378365481960832	696 ± 63	4610 ± 85	38.78 ± 4.41	16.43	2.11 ± 0.63	25.63 ± 5.26	bI!	
OBJ-15	3216174629116142336	520 ± 46	186100 ± 88	27.18 ± 1.67	11.82	1.85 ± 0.34	10.54 ± 4.66	bI	
OBJ-22	3017382033474172800	549 ± 48	8710 ± 60	14.57 ± 1.28	13.69	0.97 ± 0.30	0.52 ± 3.64	bI	✓

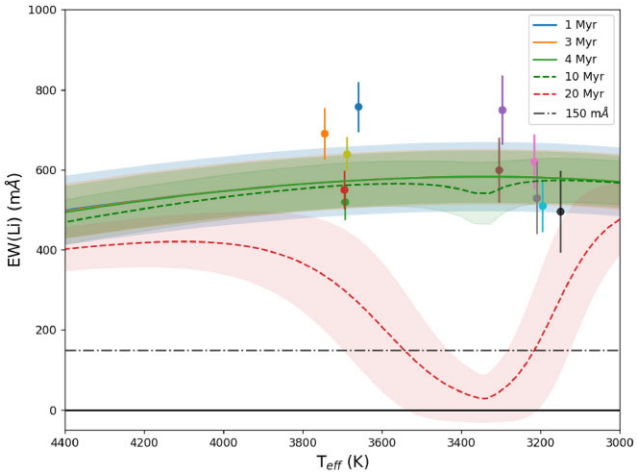

Figure 3. Effective temperature (T_{eff}) versus equivalent-width of Li (EW(Li)) for 11 runaway candidates that meet our spectroscopic youth criteria. Coloured lines are EAGLES Li depletion models (Jeffries et al. 2023) for 1, 3, 4, 10, and 20 Myr, with the shaded regions indicating their 1σ uncertainty. T_{eff}s were estimated by comparison to PARSEC (Marigo et al. 2017) stellar evolution models on a de-reddened Gaia DR3 BP-RP v G-RP colour-colour diagram (see Section 3.1.1).

Out of 27 observed targets, we found 11 stars with EW(Li) above the thresholds commonly used for YSO signatures (e.g. EW(Li) > 0.1–0.2 Å, Jeffries et al. 2014; Armstrong et al. 2020, 2022). EW(Li) for each of these 11 targets is notably large, ranging from 0.44 Å for the smallest to 0.81 Å for the largest. In Fig. 3, we plotted the effective temperature (estimated by comparing position in a de-reddened *Gaia* DR3 BP−RP versus G–RP colour–colour diagram with PARSEC (Marigo et al. 2017) stellar evolution models, using extinction and reddening estimates for each source, taken from Farias et al. 2020.) versus EW(Li) for these targets. And based on comparison to the EAGLES Lithium depletion model (Jeffries et al. 2023), our targets are consistent with ages < 10 Myr.

We also found 5 stars that exhibit EW(H α) above the thresholds commonly used for YSO signatures (e.g. EW(H α) > 10 Å, Nikoghosyan & Azatyan 2019; Armstrong et al. 2022), which are all among the candidates with high EW(Li)s. In the 11 Li-rich candidates, EW(H α) varies from a minimum of 4.56 Å to a maximum of 18.61 Å.

In Fig. 2, we present the detected H α emission line and Li 6708 Å profile. In conclusion, we confirm that 11 out of 27 targets are YSOs based on the presence of lithium in their optical spectra. In addition half of these YSOs have H α emission, which may indicate accretion activity.

3.1.2 *Variability*

Out of the 27 observed runaway candidates 12 meet the VARflag criteria of Farias et al. (2020): OBJ-2, 5, 7, 9, 12, 14, 15, 16, 19, 21, 22, and 23. Out of these, however, OBJ-16, 19, 21, and 23 were not also confirmed as YSOs by EW(Li).

Out of the 27 observed runaway candidates we found 7 that were included in the *Gaia* DR3 YSO variability catalogue (see Marton et al. 2023; Rimoldini et al. 2023), all of which were also confirmed as a YSO by EW(Li).

Interestingly, only 4 candidate runaways both meet the Farias et al. (2020) VARflag criteria and are included in the Gaia DR3 YSO variability catalogue, OBJ-2, 7, 15, and 22, all 4 of which are confirmed as YSOs by EW(Li).

3.1.3 *IR-excess*

We also used photometric measurements from 2MASS (Cutri et al. 2003) and *WISE* to identify IR excess that indicates the presence of a circumstellar disc and thus is a signature of youth. A condition used to classify the presence of IR excess is if their $K - W4$ is larger than 0.2 (Wu et al. 2013). In Fig. 4, we can see that all of the 11 Li-rich targets are well above the 0.2 threshold.

We also constructed the SEDs of each of the 11 targets using fluxes from *WISE*, 2MASS, and SDSS (Abdurro'uf et al. 2022) when available. Fig. 5 illustrates the SEDs and stellar photospheric models from Kurucz (1992) overlaid with each target. In all of the SEDs, it is clear that there is a notable increment in the flux at 2.4 μm, which indicates possible IR excess, even for the targets that are not classified as *WISE* YSO.

3.1.4 *Li-poor targets*

Among the 16 observed targets which did not show strong Li or H α features, the target ID3018141830356350976 (OBJ-20) in particular, is located above the Baraffe et al. (2015) 1 Myr isochrone (see Fig. A1), yet only has an EW(Li) of 81.93 ± 25.25 mÅ (see Fig. A2).

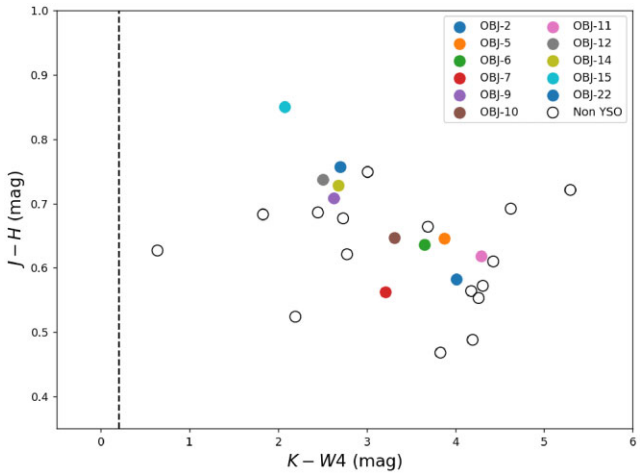

Figure 4. Diagram of *J–H* versus *K–W4* of the runaway candidates, where coloured points indicate our 11 confirmed YSOs. The black dashed line illustrates the threshold for IR excess.

Possible reasons why this source appears young in the CMD could be inaccurate reddening and extinction, and/or binarity. The other Li-poor targets, while showing other indications of youth, such as evidence of IR-excess, are generally located well below the Li-rich targets in CMDs, in closer proximity to 20 and 30 Myr isochrones. They have likely either depleted most of their photospheric Li at this age, or else are older still but have inaccurate reddening and extinction, making them appear younger in the CMD.

3.2 Radial velocities and 3D traceback

The 11 targets with detected lithium were cross-correlated with matching synthetic spectra and RVs were determined from the position of the peak in the cross-correlation function (CCF) by fitting a Gaussian function. Synthetic spectra were produced using the MOOG spectral synthesis code (Sneden et al. 2012), with Kurucz (1992) solar-metallicity model atmospheres, for log $g = 4.0$ from $T_{\rm eff} = 7000$ K down to $T_{\rm eff} = 3500$ K in 500 K steps.

To perform the RV measurement we use IRAF `rvsao` package (Mink & Kurtz 1998). We computed the heliocentric velocity corrections using the IRAF `rvcorrect` task. RV uncertainties were determined empirically from the difference in RV between n separate exposures of the same target ($\Delta v_r = (v_{r,\rm max} - v_{r,\rm min})/\sqrt{n}$). Heliocentric RV ($v_r$) and uncertainties are given in Table 2.

Now that we have confirmed 11 of our runaway candidates as YSOs via spectroscopic youth signatures and have measured v_r for them, we can trace back their past trajectories in 3D to confirm their possible origin in the ONC and estimate the time since their ejection from the cluster.

We begin, as in Farias et al. (2020), by defining the reference frame of the ONC. We adopt the central coordinates of the cluster as RA $= 05h35m16.26s$, Dec. $= -05d23m16.4$s and the distance as 403 pc (Da Rio et al. 2016). We adopt an ONC proper motion of $\mu_{\alpha*} = 1.43 \pm 0.14$ mas yr^{-1} and $\mu_\delta = 0.52 \pm 0.12$ mas yr^{-1} from Kuhn et al. (2019) and cluster mean v_r of 26.4 ± 1.6 km s^{-1} from Farias et al. (2020), Da Rio, Tan & Jaehnig (2014), and Hoogerwerf et al. (2001). For the calculation of 3D trajectories, observed astrometry and radial velocities for each runaway candidate, as well as the ONC frame, were transformed into 3D Cartesian positions and velocities X, Y, Z, U, V, W (along with their associated uncertainties) to eliminate the need for corrections of perspective effects caused by a spherical coordinate system and the motion of the Sun therein.

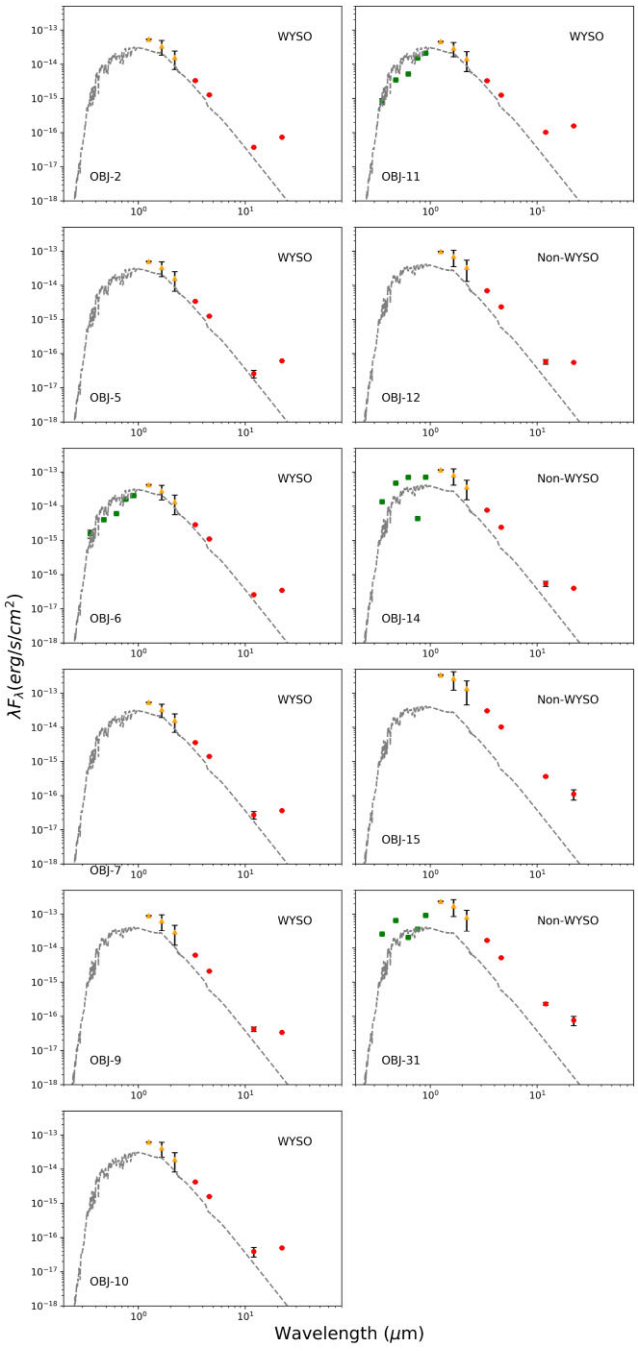

Figure 5. SEDs of the targets, showing the optical SDSS *ugriz* (green squares; when available), 2MASS *JHK* (yellow triangles), and *WISE W1, W2, W3, W4* (red dots) fluxes. A Kurucz photosphere model for the given temperature is displayed (dashed lines) to clarify the possible presence of an IR excess.

As in Farias et al. (2020), 3D traceback is performed using vector algebra. To find the time and distance of closest approach to the center of the ONC we use

$$\tau_{\rm min,3D} = -\frac{(X_* - X_0)\dot{(}V_* - V_0)}{|V_* - V_0|^2} \quad (1)$$

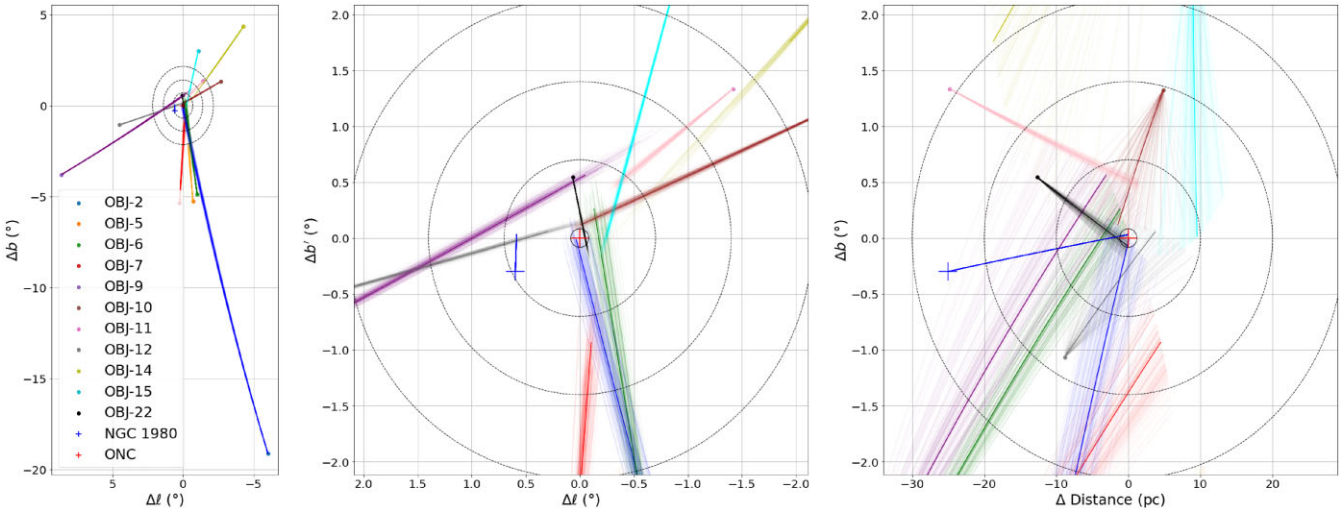

Figure 6. *Left*: Positions relative to the ONC of spectroscopically confirmed YSOs and their plane-of-sky trajectories from the position of 3D closest approach to the ONC. Solid lines indicate the median trajectory, faint lines indicate 100 trajectories per runaway calculated with random contributions from their proper motion and radial velocity errors, assuming a fixed distance. Dashed circles indicate concentric radii centred on the ONC at radial distances of 10, 20, and 30 pc. The blue cross indicates the central position of NGC 1980 and its median trajectory relative to the ONC is also plotted. *Middle*: Zoomed-in on the region around the ONC. *Right:* Line-of-sight distance (pc) against Galactic latitude.

and

$$D_{\mathrm{min,3D}} = |(X_* - \tau_{\mathrm{min,3D}} V_*) - (X_0 - \tau_{\mathrm{min,3D}} V_0)|, \quad (2)$$

where X_* and V_* are the 3D position and velocity of the star and X_0 and V_0 are the 3D position and velocity of the ONC.

We find a range of 3D ejection timescales among these 11 YSOs, ranging from 0.97–4.68 Myr with a typical precision of ~ 0.5 Myr, as well as a range of closest approach distances from 0.25–25.6 pc with a typical precision of ~ 6 pc. Table 2 summarizes these results, including measured equivalent widths, radial velocities, and 3D traceback properties.

In Fig. 6, we plot the positions of the spectroscopically confirmed YSOs relative to the ONC ($\Delta\ell$, Δb, $\Delta Distance$), with solid lines to indicate their mean trajectory relative to the ONC from their point of closest approach, and faint lines to indicate the uncertainty on their trajectories, produced by Monte Carlo with 100 iterations each time adding perturbations randomly sampled from their proper motion and RV errors. The dashed circles indicate 10, 20, and 30 pc radii centered on the ONC. We also indicate the position and past motion of NGC 1980 relative to the ONC.

From the above results, we see that most of the 11 sources satisfy 3D traceback, i.e. with $D_{\mathrm{min,3D}}$ consistent with zero within 3σ, with the exception of OBJ-14. We note the radius of the ONC is estimated to be about 2.5–3 pc (Da Rio et al. 2014; Kroupa et al. 2018), therefore we can discard runaway candidates who do not trace back to a closest approach distance within this radius within their uncertainties. From this filtering process, we conclude that OBJ-14 is least likely to have been ejected from the ONC. In addition, OBJ-5 and OBJ-15 have minimum ONC approach distances that are about 2–3σ deviant from zero, which raises doubts about their origin in the ONC. Thus our finalized, highest confidence sample of ONC runaways consists of 8 sources: OBJ-2, 6, 7, 9, 10, 11, 12, 22, as indicated by the last column of Table. 2.

4 DISCUSSION

4.1 Comparison of kinematic ejection ages with isochronal ages

True YSO runaways cannot have an ejection time-scale longer than the age of the YSO itself. To double-check the feasibility of these ejection time-scales, we estimated the isochronal ages of our candidates using Baraffe (Baraffe et al. 2015), PARSEC (Marigo et al. 2017), and SPOTS (with $X = 0.90$ and $f = 0.70$) (Somers et al. 2020) models (see Fig. 7). We took into account extinction and reddening for each source, taken from Farias et al. (2020). We note that isochronal ages for low-mass YSOs estimated in this way can vary significantly depending on the stellar evolution models used (Table 3). For a given position on the colour–magnitude diagram (CMD), models that include magnetic activity, e.g. SPOTS, tend to predict older ages than models without such effects. However, at very low masses and at very young ages, the situation can reverse, with the Baraffe models predicting older ages.

Given the possibility of large systematic errors in the isochronal age estimates, we show the results from use of each model, treating this an approximate way of estimating a range of possible ages. However, the formal uncertainties in the isochronal ages are difficult to assess.

Nevertheless, we then compared our ejection time-scales to the isochronal age estimates (Fig. 7). YSOs with isochronal ages similar or older than their ejection time-scales are more likely to be old enough to have been ejected from the ONC, given their current position and velocity. On the other hand, YSOs with isochronal ages younger than their ejection time-scales should be excluded from having been ejected from the ONC. We have shaded this 'forbidden zone' in grey in Fig. 7. However, we note that uncertainties in the ejection and isochronal ages could cause stars to scatter into this forbidden zone. From this assessment, OBJ-7 is the most suspect, since its oldest isochronal age estimate (from Baraffe) is only about 60 per cent of its ejection age. Still, even here, given potential systematic uncertainties in isochronal ages, we consider that this source could still be an ONC runaway. For the remaining sources,

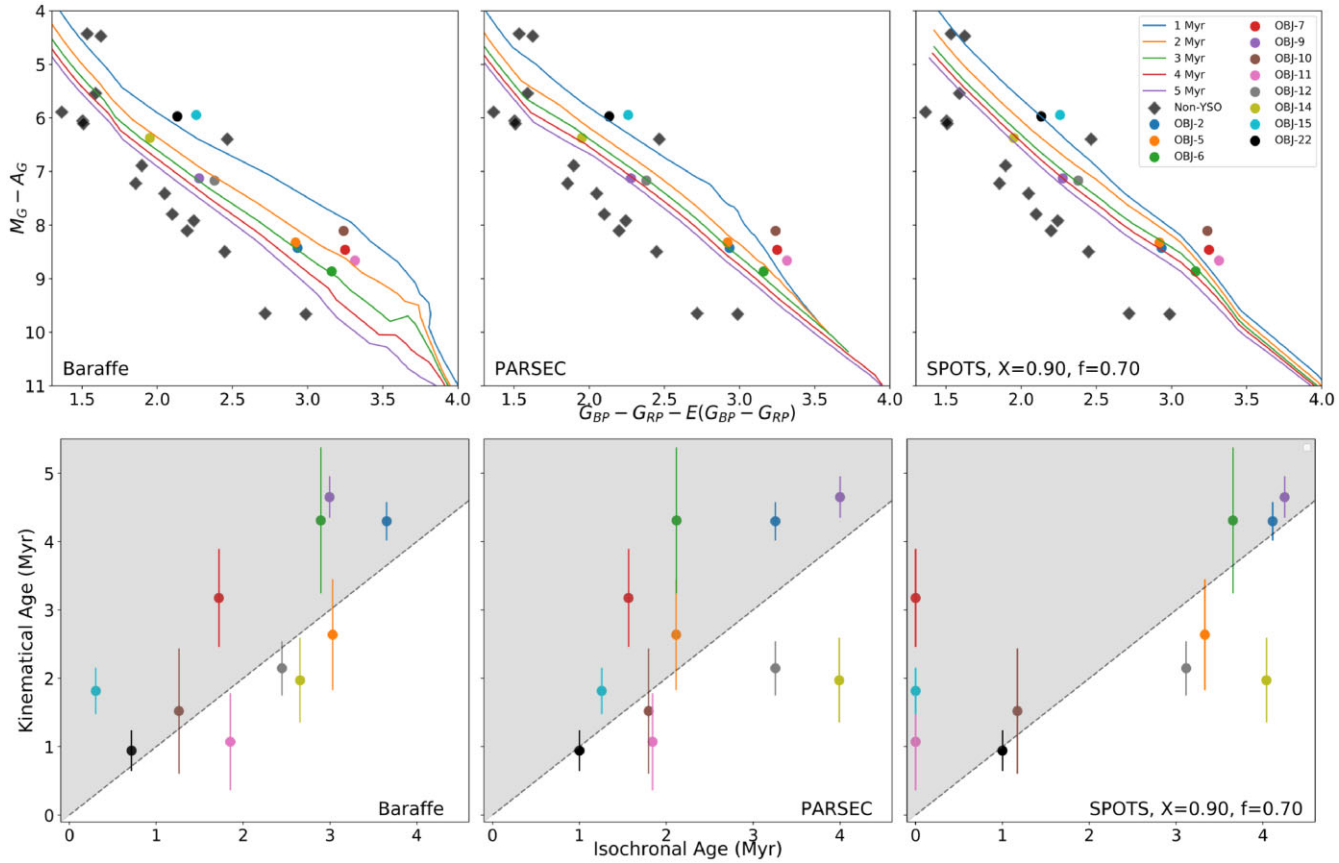

Figure 7. *Top*: Gaia DR3 BP–RP colour–MG absolute magnitude diagram for spectroscopically confirmed YSOs in our sample. Extinction AG and reddening E(BP–RP) are estimated per source from *Gaia*. Overlaid are Baraffe et al. (2015), PARSEC (Marigo et al. 2017), and SPOTS (Somers, Cao & Pinsonneault 2020, $x = 0.9, f = 0.7$) isochrones for 1, 2, 3, 4, and 5 Myr. *Bottom*: Plot of isochronal ages estimated by CMD position relative to Baraffe et al. (2015), PARSEC (Marigo et al. 2017), and SPOTS (Somers et al. 2020, $x = 0.9, f = 0.7$) isochrones–ejection time-scales for spectroscopically confirmed YSOs.

we find that isochronal age estimates are generally consistent with their ejection ages.

4.2 Confirmed ONC member

One of our runaway candidates, OBJ-22 (Gaia ID 3017382033474172800), also known as V∗ V1781 Ori, has been reported by Rebull (2001) as an M2.5 star member of the ONC. The interpolated temperature suggests that this object has a temperature of approximately 3700 K. The age estimation for this object ranges from 0.4 to 1.00 Myr. Based on our traceback calculation, the star should have been ejected 0.97 ± 0.30 Myr ago, with the closest approach to the ONC of 0.52 ± 3.64 pc, which is the second smallest among our candidates. Considering both the closest approach and time-scales of the object, it is evident that OBJ-22, or V∗1781 Ori, is not only a member of the ONC but also a relatively recent runaway star.

4.3 Alternative origin clusters

Apart from the ONC, the Orion star-forming region is a large complex consisting of many sub-regions ranging from sparse associations to dense clusters. In order to be more certain that the ONC is the origin of our runaways candidates we need to consider whether their trajectories intersect with any other young clusters, especially for candidates where their ONC ejection time-scale is greater than their isochronal age estimate.

We check the recent cluster catalogue of Hunt & Reffert (2023) for other young (<15 Myr) clusters in the region, limiting to clusters with a mean distance in a similar range as that of our YSO runaway candidates (∼ 350–420 pc). The distribution of their members on the sky is shown in Fig. 8 along with the positions and trajectories of the YSOs and the position of the ONC. We note that none of our YSO runaway candidates are included as members of any of these clusters in this catalogue. We also plot other candidate YSOs in the region, either from the *Gaia* DR3 variable source catalogue (Marton et al. 2023), APOGEE targets from Kounkel et al. (2018) or candidate young stars identified by Prisinzano et al. (2022), as grey points.

Using cluster central positions, proper motions, distances, and radial velocities from the catalogue, we repeat the 3D traceback analysis for our YSOs relative to these clusters. In particular, we find that OBJ-14 has a $D_{\mathrm{min,3D}} = 8.85 \pm 5.31$ pc and $\tau_{\mathrm{min,3D}} = 1.24 \pm 0.45$ Myr relative to the σ Ori cluster (green in Fig. 8), making it much more likely to be a runaway from the σ Ori cluster (2.8 Myr, 46 members; Kounkel et al. 2022) than the ONC. Also, we find that OBJ-9 has a $D_{\mathrm{min,3D}} = 3.05 \pm 6.04$ pc and $\tau_{\mathrm{min,3D}} = 4.26 \pm 0.32$ Myr relative to the NGC 1980 cluster (blue cross in Fig. 6, blue in Fig. 8), though both of these values are similar to those calculated when tracing from the ONC. We also find that OBJ-6 has a $D_{\mathrm{min,3D}} = 5.96 \pm 12.39$ pc and $\tau_{\mathrm{min,3D}} = 3.79 \pm 0.14$ Myr relative to NGC 1980 (3.1 Myr, 34 members; Kounkel et al. 2022). The argument can be made that the ONC, being the more massive

Table 3. Isochronal ages and masses of each spectroscopically confirmed YSO estimated from Baraffe et al. (2015), PARSEC (Marigo et al. 2017), and SPOTS (Somers et al. 2020, $x = 0.9, f = 0.7$) isochrones.

ID	Gaia ID	Baraffe age (Myr)	Baraffe mass ($M_\odot$)	PARSEC age (Myr)	PARSEC mass ($M_\odot$)	SPOTS age (Myr)	SPOTS mass ($M_\odot$)
OBJ-2	3192134597649605376	3.65	0.24	3.25	0.28	4.11	0.28
OBJ-5	3207501131641282176	3.03	0.24	2.11	0.28	3.33	0.28
OBJ-6	3208291783581908608	2.89	0.18	2.12	0.19	3.65	0.22
OBJ-7	3207022053810350976	1.72	0.17	1.56	0.35	$\ll$1	0.20
OBJ-9	2984454031031531008	2.99	0.42	4.00	0.58	4.25	0.51
OBJ-10	3216889827071056896	1.26	0.18	1.79	0.63	1.17	0.43
OBJ-11	3215804677813294976	1.85	0.16	1.84	0.36	$\ll$1	0.19
OBJ-12	3012142379518284288	2.45	0.39	3.25	0.51	3.11	0.46
OBJ-14	3219378365481960832	2.65	0.56	3.99	0.69	4.03	0.75
OBJ-15	3216174629116142336	0.30	0.50	1.25	0.73	$\ll$1	0.45
OBJ-22	3017382033474172800	0.71	0.45	1.00	0.55	1.00	0.53

and dense cluster ($> 10^4\,M_\odot\,pc^{-3}$; see Hillenbrand 1997), will have many more dynamical interactions between its members and thus will eject many more runaways than NGC 1980, making OBJ-9 and 6 more likely to have originated from the ONC.

To better quantify this hypothesis, we make an estimate of the central density of the NGC 1980 cluster. We have taken the sample of 364 members of NGC 1980 from the Hunt & Reffert (2023) catalogue and estimated masses for these by comparison to a $5 Myr$ PARSEC (Marigo et al. 2017) isochrone, which we then use to extrapolate the total cluster mass ($\sim 340 \pm 40\,M_\odot$) and number of stars ($\sim$ 1050) from a Maschberger (2013) IMF. We then use the total number of stars to scale the radial profile of NGC 1980 members from Hunt & Reffert (2023). We estimate a central projected number density of $\sim 10^2\,pc^{-2}$ in NGC 1980, which is $\sim$ 5–10 times smaller than typical estimates for the ONC (see fig. 8 of Farias & Tan 2023; 5×10^2–$10^3\,pc^{-2}$). Assuming, conservatively, that the difference in 3D number density is at a similar level (note, that estimates of the 3D number density in the centre of the ONC are at a level of $\sim 10^4\,pc^{-3}$; Hillenbrand 1997), then this difference would then imply 25–100 times lower rate of dynamical interactions in NGC 1980 than in the ONC. Furthermore, considering the total numbers of stars ($\sim$ 1050 for NGC 1980, $\sim$ 3500 for the ONC; Hillenbrand 1997), implies $\sim$ 80–350 times fewer ejections from NGC 1980 compared to from the ONC. Thus, any candidate runaway whose trajectory is consistent with originating in either NGC 1980 or the ONC is much more likely to have originated from the ONC.

We also check for matches between our YSO runaway candidates and the runaway candidate catalogue of Kounkel et al. (2022) and the clusters/subclusters they trace from in the plane-of-sky. OBJ-2 is included as a possible runaway from their Rigel subcluster (5.7 Myr, 24 members; Kounkel et al. 2022), OBJ-10 is included as a possible runaway from epsilon Ori-2 (3.8 Myr, 33 members; Kounkel et al. 2022), OBJ-11 is included as a possible runaway from NGC 1977 (2.6 Myr, 22 members; Kounkel et al. 2022), OBJ-12 from LDN 1647 (2.1 Myr, 86 members; Kounkel et al. 2022) and OBJ-14 from OriCC-9 (3.6 Myr, 26 members; Kounkel et al. 2022). None of our YSO runaway candidates match with their cluster/subcluster members.

LDN 1647 has a mean parallax of 2.284 mas ($\sim$437 pc), and has 23 members with RVs available from SOS (Tsantaki et al. 2022) giving a mean cluster v_r of 20.55 km s^{-1} with a dispersion of 1.01 km s^{-1}. OBJ-12 has a distance of $386.4^{+4.5}_{-4.3}$ pc (Bailer-Jones et al. 2021) and an v_r of 21.88 ± 2.42 km s^{-1} and is thus unlikely to have originated from LDN 1647 as an $\sim$3 Myr old YSO would need to travel at $\sim$17 km s^{-1} relative to the cluster to achieve a relative distance of $\sim$50 pc in the line of sight. In fact, OBJ-12 is likely to be moving towards LDN 1647 in the line of sight and therefore cannot have originated from it.

NGC 1977 has a mean parallax of 2.572 mas ($\sim$389 pc), and has 8 members with RVs available from SOS giving a mean cluster v_r of 30.10 km s^{-1} with a dispersion of 0.91 km s^{-1}. OBJ-11 has a distance of $370.9^{+10.8}_{-10.3}$ pc (Bailer-Jones et al. 2021) and an v_r of 3.54 ± 0.81 km s^{-1} and is thus moving away from the cluster at a relative velocity of 26.56 km s^{-1}. Therefore, if OBJ-11 was ejected from NGC 1977 it would have an ejection time-scale of $\sim$ 0.68 Myr.

OriCC-9 and epsilon Ori-2 have only 2 members with RVs from SOS (Tsantaki et al. 2022) and the Rigel subcluster only 1, making it difficult to determine their group 3D kinematics. Thus, we cannot entirely dismiss these groups as possible origins of OBJ-2, OBJ-10, and OBJ-14. But again, we reiterate that as the most massive cluster, the ONC is the more likely origin for candidate runaways in general when we cannot compare precise 3D trajectories.

We also note that OBJ-5, OBJ-6, OBJ-7, and OBJ-22 are included among the 14 832 members of the Orion cluster 606 of Prisinzano et al. (2022), while our other YSO runaway candidates are not included in any cluster of theirs. However, as shown in Fig. 8, OBJ-5, OBJ-6, and OBJ-7 are not clearly affiliated at present with any dense cluster or substructure within the Orion region. Thus, given their 3D trajectories, and relative velocities ($v_{3D,ONC} >$12 km s^{-1}), we can conclude that they are likely ONC runaways rather than being members of the sparsely distributed and dispersing population.

Apart from the likely origin of OBJ-14 from the σ Ori cluster, we do not find more likely origin clusters in the Orion region for our runaway candidates than the ONC, on the basis of 3D closest approach analysis and given the much greater rate of ejections expected from the ONC compared to other clusters in the region. In particular, we do not find more likely alternative clusters of origin for our confirmed YSO candidates with the longest ejection timescales OBJ-2, OBJ-6, and OBJ-9, strengthening the evidence that they originated from the ONC.

4.4 New oldest runaways and implications for star formation efficiency per free-fall time

Among our very likely runaway candidates, we noted that several have relatively old ejection ages. In particular: OBJ-2 has an ejection age of 4.40 ± 0.27 Myr (and SPOTS isochronal age of 4.11 Myr); OBJ-6 has an ejection age of 4.34 ± 1.07 Myr (and SPOTS isochronal age of 3.65 Myr); and OBJ-9 has an ejection

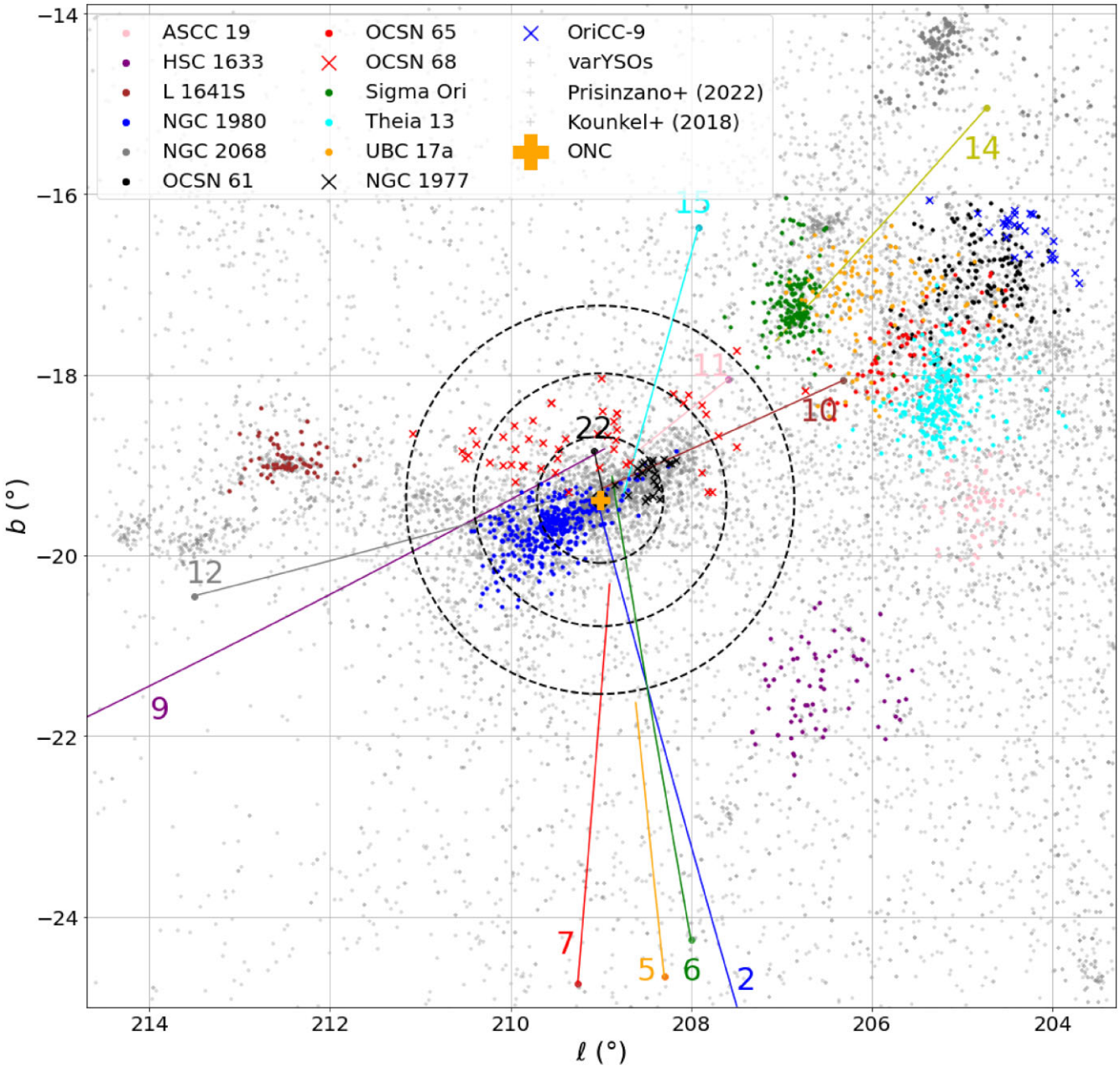

Figure 8. Positions in Galactic coordinates of spectroscopically confirmed YSOs and their plane-of-sky trajectories from the position of closest approach to the ONC. Dashed circles indicate concentric radii centred on the ONC at radial distances of 10, 20, and 30 pc. Coloured points and crosses indicate members of other nearby young (< 15 Myr) clusters in the region at mean distances between 350 and 420 pc from Hunt & Reffert (2023) and Kounkel et al. (2022), grey points are YSOs from the *Gaia* DR3 variable source catalogue (Marton et al. 2023), APOGEE targets from Kounkel et al. (2018) or candidate young stars identified by Prisinzano et al. (2022).

age of 4.68 ± 0.31 Myr (and SPOTS isochronal age of 4.25 Myr). These ejection ages are longer than those of the oldest known ONC runaways to date, i.e. μ Col and AE Aur, with an ejection time-scale of 2.5 Myr (Hoogerwerf et al. 2001).

Thus, assuming that it indeed formed in the ONC and was then ejected, OBJ-9 would set a new record for the oldest detected runaway star from the ONC. It also establishes a new lower limit for the age of the ONC itself, i.e. 4.68 ± 0.31 Myr.

This new lower limit for the age of the ONC has implications for the global star formation history, including star formation rates and efficiencies from the natal gas clump, which are important constraints on models of star cluster formation. Following Tan et al. (2006) and Da Rio et al. (2014), we estimate the star formation efficiency per free fall time as $\epsilon_{\rm ff} = 0.9\epsilon_* t_{\rm ff}/t_{\rm form,90}$. We adopt $t_{\rm ff} \simeq 0.5$ Myr, based on the dynamical mass model of Da Rio et al. (2014) at about the half-mass radius of 1.3 pc. Similarly, based on their models, we assume ϵ_*, i.e. the overall fraction of gas that has formed stars, to be $\simeq 0.5$ (including allowance for some already expelled gas). We set the time-scale for cluster formation, i.e. to form 90 per cent of the stars, to be our longest ejection age, i.e. 4.68 Myr. Thus we estimate

$\epsilon_{\rm ff} \simeq 0.048$, which is valid at the half-mass radius scale. The value of $\epsilon_{\rm ff}$ is expected to be smaller at interior radii, where the densities are higher and the free-fall time decreases.

We note that our estimate of $\epsilon_{\rm ff}$ is similar to that of Da Rio et al. (2014), which is a reflection of the fact that our oldest ejection age is similar to their estimate of isochronal age spreads in the ONC. It should also be noted that the ejection of OBJ-9 4.7 Myr ago would already have required the presence of a dense, relatively massive stellar system, i.e. at least a triple system from which it is typically the lowest mass member, i.e. OBJ-9, that is ejected. Such a triple system would have required some time to form, i.e. if it involves 10 $M_\odot$ of stars forming from a core in a $\Sigma_{\rm cl} = 0.3$ g cm^{-2} environment, then a formation time of 2.4×10^5 yr is expected (McKee & Tan 2003). In addition, from statistical considerations it is likely that additional stars in the proto-ONC would have already been forming before the particular system that ejected OBJ-9. Thus star formation is likely to have been proceeding in the ONC for longer than 4.7 Myr. Since star formation continues today in the ONC and is expected to do so at least into the near future, it is reasonable to estimate a total duration of star cluster formation that is > 5 Myr for the ONC. Our above estimate for $\epsilon_{\rm ff} \simeq 0.048$ already accounts for a fraction of star formation, i.e. 10 per cent, being outside the range measured by the ejection age of OBJ-9 to the present day. However, if this fraction is larger, then our estimate of $\epsilon_{\rm ff}$ should be regarded as an upper limit.

5 SUMMARY AND CONCLUSIONS

We have presented follow-up spectroscopic observations of 27 high-priority runaway star candidates from the ONC, based on the 2D (proper motion) traceback analysis of Farias et al. (2020), and with the targets selected as showing some indicators of youth, i.e. IR excess and/or variability. The targets were also selected to have relatively old ejection ages, which would place new constraints on the star formation history of the ONC. The primary objective of our work has been to confirm whether these targets are indeed YSOs, primarily by the presense of Li, and, by RV measurement, further confirm an origin in the ONC via 3D traceback.

The candidates were observed using the Magellan 2 + MIKE spectrograph, providing spectra to identify YSO signatures, such as lithium absorption and H α emission, and allowing for 3D traceback based on the measured radial velocity. A summary of our main results is as follows:

(i) We identified 11 out of 27 targets that exhibit significant lithium absorption (with 5 of these also showing H α emission), confirming their status as low-mass YSOs.

(ii) We are able to traceback these confirmed YSOs in 3D and revealed that 8 of the 11 YSOs have a closest approach consistent with an origin in the ONC ($D_{\rm min,3D} < 2.5$–3 pc; see Section 3.2).

(iii) We cross-match our confirmed YSO runaway candidates with several recent catalogues of clusters, star-forming regions and candidate runaways (Kounkel et al. 2022; Prisinzano et al. 2022; Hunt & Reffert 2023) to check for alternative possible origins for our candidates other than the ONC. We find that one of our confirmed YSOs, OBJ-14, is more likely to have originated from the σ Ori cluster given its 3D trajectory and isochronal age, but our runaway candidates with the longest ejection time-scales, OBJ-2, OBJ-6, and OBJ-9, are more likely to originate from the ONC than any other nearby young cluster, given the much greater rate of ejections expected from the ONC compared to other clusters in the region.

(iv) Comparing isochronal ages with ejection ages, we find general consistency in the population, but note that the variation among isochronal estimates is large, indicating potentially large systematic uncertainties. We consider that our good runaway candidates from the ONC have utility in helping to refine and calibrate pre-main-sequence models.

(v) Among the likely runaway candidates, we identified three with ejection time-scales greater than 4 Myr, with the oldest, OBJ-9, being about 4.7 Myr. Consider previous star formation before the ejection and that star formation in the ONC is still ongoing, this implies that the overall formation time of the ONC is likely to be at least 5 Myr. This corresponds to about 10 free-fall times of the system (evaluated at the half-mass radius), indicating a scenario of relatively slow, quasi-equilibrium star cluster formation (Tan et al. 2006).

(vi) The oldest ejection age of the sample of 4.7 Myr allows a new estimate of the likely mean star formation efficiency per free-fall time of $\bar{\epsilon}_{\rm ff} \simeq 0.05$. This is similar to the previous estimate of Da Rio et al. (2014), but is now independent of isochronal age estimates based on pre-main-sequence evolutionary tracks. The relatively small value of $\bar{\epsilon}_{\rm ff}$ indicates that star formation has proceeded in a relatively slow and inefficient manner, which likely indicates a role for magnetic fields and/or protostellar outflow feedback in regulating its rate (e.g. Nakamura & Li 2007).

ACKNOWLEDGEMENTS

MF acknowledges support from the CASSUM program at Chalmers Univ. of Technology. JA and JCT acknowledge support from ERC Advanced Grant MSTAR. This work has made use of data from the ESA space mission *Gaia* (http://www.cosmos.esa.int/gaia), processed by the *Gaia* Data Processing and Analysis Consortium (DPAC, http://www.cosmos.esa.int/web/gaia/dpac/consortium). Funding for DPAC has been provided by national institutions, in particular the institutions participating in the Gaia Multilateral Agreement. This research made use of the Simbad and Vizier catalogue access tools (provided by CDS, Strasbourg, France), Astropy (Astropy Collaboration 2013), and TOPCAT (Taylor 2005).

DATA AVAILABILITY

The data underlying this article will be shared on reasonable request to the corresponding author.

REFERENCES

Abdurro'uf et al., 2022, ApJS, 259, 35
Armstrong J. J., Wright N. J., Jeffries R. D., Jackson R. J., 2020, MNRAS, 494, 4794
Armstrong J. J., Wright N. J., Jeffries R. D., Jackson R. J., Cantat-Gaudin T., 2022, MNRAS, 517, 5704
Astropy Collaboration, 2013, A&A, 558, A33
Bailer-Jones C. A. L., Rybizki J., Fouesneau M., Demleitner M., Andrae R., 2021, AJ, 161, 147
Baraffe I., Homeier D., Allard F., Chabrier G., 2015, A&A, 577, A42
Bobylev V. V., Bajkova A. T., 2021, Astron. Lett., 47, 224
Cayrel R., 1988, in Cayrel de Strobel G., Spite M., eds, Proc. IAU Symp. Vol. 132, The Impact of Very High S/N Spectroscopy on Stellar Physics. Kluwer, Dordrecht, p. 345
Cody A. M., Hillenbrand L. A., 2014, ApJ, 796, 129
Cutri R. M. et al., 2003, VizieR Online Data Catalog. p. II/246
Da Rio N., Tan J. C., Jaehnig K., 2014, ApJ, 795, 55
Da Rio N. et al., 2016, ApJ, 818, 59
Elmegreen B. G., Efremov Y., Pudritz R. E., Zinnecker H., 2000, Protostars and Planets IV. p. 179
Farias J. P., Tan J. C., 2023, MNRAS, 523, 2083

Farias J. P., Tan J. C., Chatterjee S., 2019, MNRAS, 483, 4999
Farias J. P., Tan J. C., Eyer L., 2020, ApJ, 900, 14
Gaia Collaboration, 2021, A&A, 649, A1
Hillenbrand L. A., 1997, AJ, 113, 1733
Hoogerwerf R., de Bruijne J. H. J., de Zeeuw P. T., 2001, A&A, 365, 49
Hunt E. L., Reffert S., 2023, A&A, 673, A114
Jeffries R. D. et al., 2014, A&A, 563, A94
Jeffries R. D. et al., 2023, MNRAS, 523, 802
Kounkel M. et al., 2018, AJ, 156, 84
Kounkel M., Mcbride A., Stassun K. G., Leigh N., 2022, MNRAS, 517, 1946
Kroupa P., Jeřábková T., Dinnbier F., Beccari G., Yan Z., 2018, A&A, 612, A74
Kuhn M. A., Hillenbrand L. A., Sills A., Feigelson E. D., Getman K. V., 2019, ApJ, 870, 32
Kurucz R. L., 1992, in Barbuy B., Renzini A., eds, Proc. IAU Symp. Vol. 149, The Stellar Populations of Galaxies. Kluwer, Dordrecht, p. 225
Lada C. J., Lada E. A., 2003, ARA&A, 41, 57
Leonard P. J. T., Duncan M. J., 1990, AJ, 99, 608
Lindegren L. et al., 2021, A&A, 649, A2
Marigo P. et al., 2017, ApJ, 835, 77
Marks M., Kroupa P., 2012, A&A, 543, A8
Marton G. et al., 2019, MNRAS, 487, 2522
Marton G. et al., 2023, A&A, 674, A21
Maschberger T., 2013, MNRAS, 429, 1725
McBride A., Kounkel M., 2019, ApJ, 884, 6
McKee C. F., Tan J. C., 2003, ApJ, 585, 850
Mink D. J., Kurtz M. J., 1998, in Albrecht R., Hook R. N., Bushouse H. A., eds, ASP Conf. Ser. Vol. 145, Astronomical Data Analysis Software and Systems VII. Astron. Soc. Pac., San Francisco, p. 93
Nakamura F., Li Z.-Y., 2007, ApJ, 662, 395
Nikoghosyan E. H., Azatyan N. M., 2019, PASA, 36, e039
Oh S., Kroupa P., 2016, A&A, 590, A107
Parker R. J., Wright N. J., Goodwin S. P., Meyer M. R., 2014, MNRAS, 438, 620
Perets H. B., Šubr L., 2012, ApJ, 751, 133
Platais I. et al., 2020, AJ, 159, 272
Prisinzano L. et al., 2022, A&A, 664, A175
Rebull L. M., 2001, AJ, 121, 1676
Rimoldini L. et al., 2023, A&A, 674, A14
Schoettler C., 2022, PhD thesis, Univ. Sheffield
Schoettler C., Parker R. J., Arnold B., Grimmett L. P., de Bruijne J., Wright N. J., 2019, MNRAS, 487, 4615
Schoettler C., de Bruijne J., Vaher E., Parker R. J., 2020, MNRAS, 495, 3104
Schönrich R., Binney J., Dehnen W., 2010, MNRAS, 403, 1829
Sneden C., Bean J., Ivans I., Lucatello S., Sobeck J., 2012, Astrophysics Source Code Library, record ascl:1202.009
Soderblom D. R., 2010, ARA&A, 48, 581
Somers G., Cao L., Pinsonneault M. H., 2020, ApJ, 891, 29
Tan J. C., Krumholz M. R., McKee C. F., 2006, ApJ, 641, L121
Taylor M. B., 2005, in Shopbell P., Britton M., Ebert R., eds, ASP Conf. Ser. Vol. 347, Astronomical Data Analysis Software and Systems XIV. Astron. Soc. Pac., San Francisco, p. 29
Tetzlaff N., Neuhäuser R., Hohle M. M., 2011, MNRAS, 410, 190
Tsantaki M. et al., 2022, A&A, 659, A95
Wu C.-J., Wu H., Lam M.-I., Yang M., Wen X.-Q., Li S., Zhang T.-J., Gao L., 2013, ApJS, 208, 29

APPENDIX A: ID 3018141830356350976 (OBJ-20)

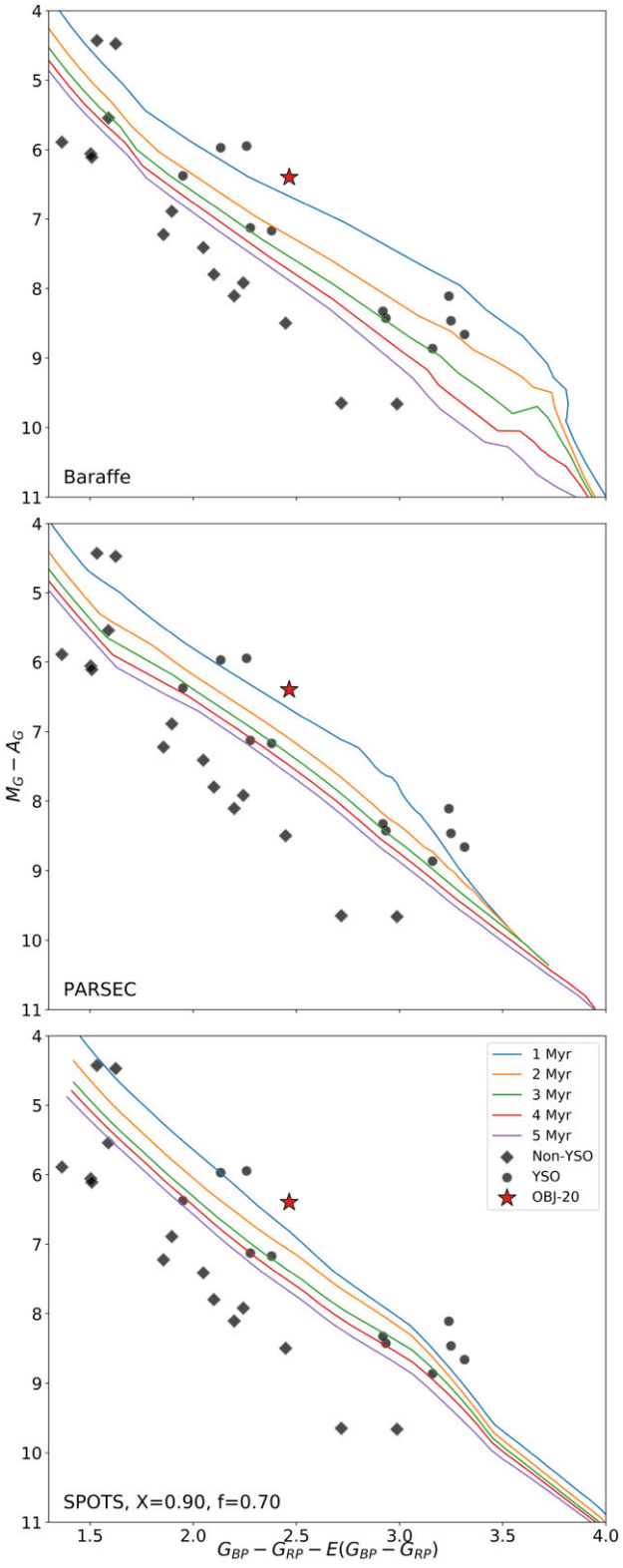

Figure A1. *Gaia* DR3 BP–RP colour–MG absolute magnitude diagram for OBJ-20 and the rest of our sample including the spectroscopically confirmed YSOs. Extinction AG and reddening E(BP–RP) are estimated per source from *Gaia*. Overlaid are Baraffe et al. (2015), PARSEC (Marigo et al. 2017), and SPOTS (Somers et al. 2020, $x = 0.9$, $f = 0.7$) isochrones for 1, 2, 3, 4, and 5 Myr.

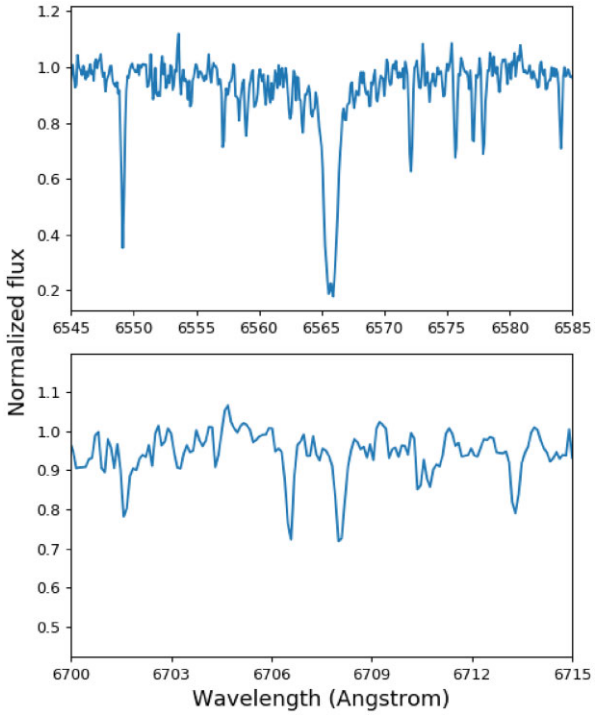

Figure A2. H α (*top)* and lithium 6708 Å (*bottom*) lines for OBJ-20. The fluxes are normalized non-calibrated counts.

This paper has been typeset from a TEX/LATEX file prepared by the author.